GEOPHYSICS, VOL. 89, NO. 5 (SEPTEMBER-OCTOBER 2024); P. MR297–MR307, 11 FIGS., 2 TABLES.
10.1190/GEO2023-0625.1

Check for updates

Downloaded 09/13/24 to 180.201.128.221. Redistribution subject to SEG license or copyright; see Terms of Use at http://library.seg.org/page/policies/terms
DOI:10.1190/geo2023-0625.1

Reflection, transmission, and AVO response of inhomogeneous plane waves in thermoporoelastic media with two-temperature equations of heat conduction

Wanting Hou[1], Li-Yun Fu[2], and José M. Carcione[3]

ABSTRACT

We develop a modified fluid-saturated thermoporoelastic model by introducing two temperature equations to account for the temperature differences between the solid skeleton and the pore filling. The modified two-temperature generalized thermoporoelastic (TTG) equation is an extension of the classical single-temperature Lord-Shulman (LS), Green-Lindsay, and generalized LS theories. It predicts four compressional waves and one shear wave based on the analysis of inhomogeneous plane waves. We study the exact reflection and transmission (R/T) coefficients at the interface separating two thermoporoelastic half-spaces and develop an amplitude-variation-with-offset (AVO) approximation. Comparison with the Biot poroelastic case of the water/oil contact shows that the TTG model reproduces the exact R/T results. The AVO response of oil, gas, and real CO_2 geosequestration reservoirs illustrates the practical applicability of our model and provides the theoretical basis for the exploration of high-temperature resources.

INTRODUCTION

Elastic wave propagation analysis in fluid-saturated, high-pressure, high-temperature fields is among the most important and effective methods for georesource exploration, from geothermal (Poletto et al., 2018; Cheng et al., 2023) to hydrocarbons (Sharma, 2008; Carcione et al., 2019). Successful explanation and interpretation of deep resources require a valid and simple model of rock physics that combines the porous properties and thermal nature of rocks. In principle, thermoporoelastic models have been extensively used to describe these deposits to better and more quantitatively evaluate temperature-dependent resource characteristics (Sharma, 2018; Hou et al., 2021, 2023b; Wang et al., 2021).

The theory of thermoporoelasticity introduces mechanical-thermal coupling in poroelasticity. The thermal effect itself on wave propagation is negligible because wave propagation is an adiabatic process (Landau and Lifshitz, 1986; Anderson, 1989) where there is insufficient time for heat flow during the period of wave propagation. The effect will not become important unless we have the so-called mesoscopic effect (i.e., conversion from thermal mode to P wave similar to the wave-induced local fluid flow in poroelasticity). However, such a conversion is very weak, as indicated by Zimmerman (2000), so although temperature influences the stresses and strains, the stresses and strains do not appreciably influence the temperature field. The indirect effect of temperature on wave propagation is significant because high temperatures significantly change the mineralogy and microstructure of rocks, which in turn, affects the velocity and attenuation of wave propagation. Observed geophysical data generally contain such indirect thermal effects.

Biot (1956a) sets up the equations based on the Fourier heat conduction law but this leads to unphysical results. Unlike Biot's use of elastic energy potential to derive the theory of thermoelasticity, the procedure of volume averaging is applied to the same problem (de la Cruz and Spanos, 1989; de la Cruz et al., 1993). In addition to the porous and thermal properties of the rocks, the relaxation times describing the time lag are important features that determine the success of the theories (Noda, 1990; Nield and Bejan, 2006). Quiroga-Goode et al. (2005) simulate wave propagation in homogeneous dynamic-porosity media with thermal and fluid relaxation. Lord and Shulman (1967) (LS) propose a more general formulation with a single temperature and one relaxation lag term (ST-LS), and Green and Lindsay (1972) present thermoelastic constitutive relations with

Manuscript received by the Editor 24 October 2023; revised manuscript received 29 April 2024; published ahead of production 23 May 2024; published online 2 September 2024.
[1]China University of Petroleum (East China), National Key Laboratory of Deep Oil and Gas, Qingdao, China. E-mail: hwtupc@163.com.
[2]China University of Petroleum (East China), National Key Laboratory of Deep Oil and Gas, Qingdao, China and Laoshan Laboratory, Qingdao, China. E-mail: lfu@upc.edu.cn (corresponding author).
[3]National Institute of Oceanography and Applied Geophysics – INOGS, Trieste, Italy and Hohai University, Nanjing, China. E-mail: jose.carcione@gmail.com.
© 2024 Society of Exploration Geophysicists. All rights reserved.

Downloaded 09/13/24 to 180.201.128.221. Redistribution subject to SEG license or copyright; see Terms of Use at http://library.seg.org/page/policies/terms
DOI:10.1190/geo2023-0625.1

an additional lag time (ST-GL). Dhaliwal and Sherief (1980) extend the ST-LS equation to general anisotropic media with heat sources. Carcione et al. (2019) and Wang et al. (2021) perform plane wave analysis and predict one shear and three longitudinal waves (fast P, slow P, and thermal waves) different from the poroelastic case where only the first two longitudinal waves occur (Biot, 1956b, 1962). Tzou (1995) and Chandrasekharaiah (1998) introduce microscopic effects into the macroscopic model to characterize the lag time of the temperature gradient of the fluid phase. Liu et al. (2023) incorporate the Tzou (1995) single-temperature dual-phase-lag (ST-DPL) model of heat conduction into thermoporoelasticity for finite difference numerical simulations. However, these formulations are based on the ST models, assuming only the average thermal properties and temperature of the entire rock. Youssef (2007) extends the ST-LS model to consider the temperature difference between the solid and the fluid, introduces two-phase temperatures, and develops a new two-temperature generalized LS (TTG-LS) thermoporoelastic equation. The model considers the laws of two-phase heat conduction with two temperatures separated differently. It predicts an additional slow thermal wave (T2) (Singh, 2011). Here, we propose a TTG-GL model by combining the GL model and that of Youssef (2007).

Quantitative studies of reflection and transmission (R/T) at a thermoelastic/ thermoporoelastic interface are considered by Wei et al. (2016) and Sharma (2018) based on the lossless P-wave incidence. Zhou et al. (2019), Liu et al. (2021, 2022), and Kumar et al. (2022a) study wave propagation in unsaturated thermoporoelastic media and analyze the dependence of dispersion and R/T coefficients on thermal parameters. Kumar et al. (2022b) and Kumari et al. (2022) also investigate the propagation of inhomogeneous waves in this medium and further extend their study to the double-porosity case (Kumar et al., 2023). More recently, Hou et al. (2023a) address a similar problem of inhomogeneous waves as Wang et al. (2021), studying the ST-LS, GL, and generalized LS (GLS) theories. The former focuses on a thermoporoelastic/thermoporoelastic interface, while the latter considers a free surface. The preceding R/T results are based on the exact Zoeppritz formulation, which is the basis for amplitude-variation-with-offset analysis (AVO). However, the exact calculations are cumbersome and difficult to relate to physical properties. Hou et al. (2023b) present AVO approximate thermoelastic equations based on the results of Aki and Richards (2002). The approximation of thermoporoelastic theory has not been studied previously, so we consider the approximation including the proposed LS and GL thermoporoelastic theories with the two-temperature and two-phase thermal parameters.

In this work, we first extend the ST-GL thermoporoelastic equation based on the Youssef (2007) model (TTG-GL). The analysis of inhomogeneous plane waves predicts four compressional waves and one shear wave, i.e., fast P (P1), slow P (P2), thermal (T1), slow thermal (T2), and S waves. The P2 wave is related to pressure differentials, whereas the T1 wave is primarily associated with temperature gradients. In contrast, the T2 wave combines the influences of both, resulting in similar trends but different physical properties. The R/T coefficients are obtained based on a fluid-saturated thermoporoelastic/thermoporoelastic interface and the corresponding ten boundary conditions. We then develop a thermoporoelastic approximate model that accounts for the thermal effects and compare it with Biot's poroelastic model. Finally, the AVO responses of different reservoir cases (gas saturated, oil saturated, and CO_2 geosequestration) are tested by applying the approximation. The method we proposed can be relevant for the exploration of high-temperature and high-pressure deep reservoirs in thermal hydrocarbon source rocks. Furthermore, it can provide essential guidance for conducting seismic thermoelastic inversions to evaluate subsurface temperature distribution and reservoir characteristics under high-temperature conditions.

THERMOPOROELASTICITY

Differential equations

Let us define u_i and w_i $(i = x, y, z)$ as the components of the displacement field of the frame and of the fluid relative to the frame, respectively, with T_s and T_f as the temperature increase of the solid and the fluid phases, respectively, with respect to the absolute reference temperature T_0, assuming the same T_0 for both components of the medium. In the absence of external forces and heat sources, the constitutive relations for the total stress σ_{ij} and fluid pressure p are given by Sharma (2018), Carcione et al. (2019), and Carcione (2022):

$$\begin{aligned}
&\sigma_{ij} = 2\mu\epsilon_{ij} + \lambda\epsilon_m\delta_{ij} - R_{11}(\wedge_{1s}\, T_s)\delta_{ij} - R_{12}(\wedge_{1f}\, T_f)\delta_{ij},\\
&-p = M\epsilon - R_{22}(\wedge_{1f}\, T_f) - R_{21}(\wedge_{1s}\, T_s),\\
&\epsilon = \bar{\alpha}\epsilon_m + \epsilon_f, \quad \epsilon_m = u_{i,i}, \quad \epsilon_f = w_{i,i}, \quad 2\epsilon_{ij} = u_{i,j} + u_{j,i},
\end{aligned} \tag{1}$$

where the subscripts "s" and "f" indicate solid and fluid, respectively, and δ is the Kronecker delta function. The rock frame is characterized by the porosity $\bar{\phi}$, Lamé constants μ and λ, bulk modulus K, thermal relaxation time τ, and

$$\begin{aligned}
&M = \left(\frac{\bar{\alpha} - \bar{\phi}}{K_s} + \frac{\bar{\phi}}{K_f}\right)^{-1},\\
&\bar{\alpha} = 1 - \frac{K_m}{K_s}, \quad K_m = \lambda + \frac{2}{3}\mu,\\
&\wedge_{ij} = 1 + \tau_{ij}\partial_t, \quad \wedge_{ij}^2 = \partial_t + \tau_{ij}\partial_{tt}, \quad \iota = 1, 2, 3, \quad j = s, f.
\end{aligned} \tag{2}$$

The differential equations of motion are

$$\begin{aligned}
&\sigma_{ij,j} = \rho\ddot{u}_i + \rho_f\ddot{w}_i,\\
&(-p)_{,i} = \rho_f\ddot{u}_i + m\ddot{w}_i + b\dot{w}_i,
\end{aligned} \tag{3}$$

where the composite density $\rho = (1 - \bar{\phi})\rho_s + \bar{\phi}\rho_f$ depends on the solid and fluid densities ρ_s and ρ_f, respectively. Moreover, $m = \mathcal{T}\rho_f/\bar{\phi}$, where $\mathcal{T}$ is the tortuosity, $b = \eta/\bar{\kappa}$, η is the fluid viscosity, and $\bar{\kappa}$ is the frame permeability. Substituting the stress-strain relations into equation 3, we obtain

$$\begin{aligned}
&\mu\nabla^2\mathbf{u} + E_M\nabla\epsilon_m + \bar{\alpha}M\nabla\epsilon_f - \nabla[R_{11}(\wedge_{1s}\, T_s) + R_{12}(\wedge_{1f}\, T_f)]\\
&\quad = \rho\ddot{\mathbf{u}} + \rho_f\ddot{\mathbf{w}},\\
&\bar{\alpha}M\nabla\epsilon_m + M\nabla\epsilon_f - \nabla[R_{21}(\wedge_{1s}\, T_s) + R_{22}(\wedge_{1f}\, T_f)]\\
&\quad = \rho_f\ddot{\mathbf{u}} + m\ddot{\mathbf{w}} + b\dot{\mathbf{w}}.
\end{aligned} \tag{4}$$

Downloaded 09/13/24 to 180.201.128.221. Redistribution subject to SEG license or copyright; see Terms of Use at http://library.seg.org/page/policies/terms
DOI:10.1190/geo2023-0625.1

The law of heat conduction is (Youssef, 2007)

$$\bar{\gamma}_s\nabla^2 T_s = \wedge_{2s}^2 [F_{11}T_s + F_{12}T_f + T_0(R_{11}\epsilon_m + R_{21}\epsilon_f)],$$
$$\bar{\gamma}_f\nabla^2 T_f = \wedge_{2f}^2 [F_{22}T_f + F_{21}T_s + T_0(R_{22}\epsilon_f + R_{12}\epsilon_m)], \quad (5)$$

where ∇^2 is the Laplacian operator,

$$\bar{\gamma}_s = (1-\bar{\phi})\bar{\gamma}_s^*, \quad \bar{\gamma}_f = \bar{\phi}\bar{\gamma}_f^*,$$
$$E_M = \lambda + \mu + \bar{\alpha}^2 M, \quad R_{11} = (1-\bar{\phi})\beta_s, \quad R_{12} = \bar{\alpha}\beta_f,$$
$$R_{22} = 3M\bar{\phi}\bar{\alpha}_f, \quad R_{21} = 3M(\bar{\alpha}-\bar{\phi})(1-\bar{\phi})\bar{\alpha}_s,$$
$$F_{11} = (1-\bar{\phi})c_s\rho_s, \quad F_{22} = \bar{\phi}c_f\rho_f, \quad F_{12} = F_{21} = -JT_0,$$
$$J = 3\bar{\alpha}_s R_{12} + \bar{\alpha}_{fs}R_{22}, \quad (6)$$

where c is the bulk specific heat, $\bar{\gamma}^*$ is the thermal conductivity, β is the thermoelasticity coefficient, and $\bar{\alpha}$ is the thermal expansion coefficient (Pecker and Deresiewicz, 1973; Youssef, 2007; Carcione et al., 2019).

The TTG-LS model is obtained with $\tau_{1j} = 0$ ($j = s$ or f) and $\tau_{2j} = \tau_{3j}$ (Carcione et al., 2019) (for the generalized case $\tau_{2j} \neq \tau_{3j}$), in the case of the TTG-GL equation with $\tau_{3j} = 0$, whereas the TTG-LS and TTG-GL models coincide if $\tau_{2j}^{\mathrm{LS}} = \tau_{1j}^{\mathrm{GL}}$ (Wang et al., 2021). For simplicity, TTG is omitted in the following.

Plane-wave analysis

We use the Helmholtz decomposition and consider the propagation of compressional waves (Wang et al., 2021), obtained from equations 4 and 5:

$$E_G\nabla^2\phi_s + \bar{\alpha}M\nabla^2\phi_f - [R_{11}(\wedge_{1s}T_s) + R_{12}(\wedge_{1f}T_f)] = \rho\ddot{\phi}_s + \rho_f\ddot{\phi}_f,$$
$$\bar{\alpha}M\nabla^2\phi_s + M\nabla^2\phi_f - [R_{22}(\wedge_{1f}T_f) + R_{21}(\wedge_{1s}T_s)] = \rho_f\ddot{\phi}_s + m\ddot{\phi}_f + b\dot{\phi}_f,$$
$$\bar{\gamma}_s\nabla^2 T_s = \wedge_{2s}^2(F_{11}T_s + F_{12}T_f) + T_0\nabla^2[\wedge_{3s}^2(R_{11}\phi_s + R_{21}\phi_f)],$$
$$\bar{\gamma}_f\nabla^2 T_f = \wedge_{2f}^2(F_{21}T_s + F_{22}T_f) + T_0\nabla^2[\wedge_{3f}^2(R_{12}\phi_s + R_{22}\phi_f)],$$
$$\mu\nabla^2\psi_s = \rho\ddot{\psi}_s + \rho_f\ddot{\psi}_f,$$
$$\rho_f\ddot{\psi}_s + m\ddot{\psi}_f + b\dot{\psi}_f = 0, \quad (7)$$

where $E_G = E_M + \mu$ and the potential functions and temperature fields are

$$\phi_s = A_s^{\mathrm{P}}\exp[\mathrm{i}(\mathbf{k_P}\cdot\mathbf{x} - \omega t)],$$
$$\phi_f = A_f^{\mathrm{P}}\exp[\mathrm{i}(\mathbf{k_P}\cdot\mathbf{x} - \omega t)],$$
$$T_s = A_{Ts}^{\mathrm{P}}\exp[\mathrm{i}(\mathbf{k_P}\cdot\mathbf{x} - \omega t)],$$
$$T_f = A_{Tf}^{\mathrm{P}}\exp[\mathrm{i}(\mathbf{k_P}\cdot\mathbf{x} - \omega t)],$$
$$\psi_s = A_s^{\mathrm{S}}\exp[\mathrm{i}(\mathbf{k_S}\cdot\mathbf{x} - \omega t)],$$
$$\psi_f = A_f^{\mathrm{S}}\exp[\mathrm{i}(\mathbf{k_S}\cdot\mathbf{x} - \omega t)], \quad (8)$$

where $\mathbf{x}$ is the spatial vector, $\mathbf{k_P}$ and $\mathbf{k_S}$ are the wavenumbers, and A^{P} and A^{S} are the amplitudes of the compressional and shear waves, respectively (Hou et al., 2023a; equations 5–9).

Substituting equation 8 into equation 7, we obtain

$$\sum_{\iota=0}^{4}(coe_{(2\iota)}\cdot(k_{\mathrm{P}}^2)^{\iota}) = 0, \quad (9)$$

where

$$coe_8 = EM\bar{\gamma}_s\bar{\gamma}_f,$$
$$coe_6 = \omega\{-a_{61}\bar{\gamma}_s\bar{\gamma}_f - EMa_{62} + \mathrm{i}T_0[E_G a_{64} + M(a_{65}+a_{66})]\},$$
$$coe_4 = \omega^2[a_{44} + \mathrm{i}T_0(a_{45}+a_{46}+a_{47}+a_{48}) - EMa_{63}\bar{\tau}_{s2}\bar{\tau}_{f2} - \omega a_{43}\bar{\gamma}_s\bar{\gamma}_f + a_{61}a_{62}],$$
$$coe_2 = \omega^3\{a_{62} + \mathrm{i}T_0[\omega(a_{22}+a_{23}) - (m\omega + \mathrm{i}b)(a_{24}-a_{25})]\},$$
$$coe_0 = \omega^5\bar{\tau}_{f2}\bar{\tau}_{s2}a_{63}a_{43}, \quad (10)$$

and

$$E = \lambda + 2\mu, \bar{\tau}_{ij} = \mathrm{i} + \omega\tau_{ij}. \quad (11)$$

The components of a are given in Appendix A. For an S plane wave, the wavenumber is

$$k_{\mathrm{S}}^2 = \omega^2\left[\frac{\rho}{\mu} - \frac{\omega\rho_f^2}{\mu(\omega m + \mathrm{i}b)}\right]. \quad (12)$$

The complex wavenumber and phase velocity are (Appendix A)

Table 1. Properties of the water/oil/gas saturated medium.

K_s (GPa)	K_m (GPa)	K_f (GPa)	μ (GPa)	ρ_f (g/cm^3)	ρ_s (g/cm^3)
35	7	2.4/2.1/0.0056	5.5	1.0/0.7/0.14	2.65
$\mathcal{T}$	η_f ($\times10^{-3}$) (Pa s)	$\bar{\kappa}$ (D)	$\bar{\phi}$	τ_{2f} (ns)	τ_{2s} (ns)
2	1/4/0.22	1	0.1/0.25/0.25	2.5/1.6/4	0.08
c_f ($\times10^3$) kg/(m · s^2 · K)	c_s ($\times10^3$) kg/(m · s^2 · K)	β_f ($\times10^6$) kg/(m · s^2 · K)	β_s ($\times10^6$) kg/(m · s^2 · K)	$\bar{\gamma}_f^*$ m · kg/(s^3 · K)	$\bar{\gamma}_s^*$ m · kg/(s^3 · K)
4.18/2.88/1.47	0.9	0.7/1.5/1.2	2.1	8.76/8.45/7.79	12
T_0 (K)	$\bar{\alpha}_s$ ($\times10^{-6}$) (K^{-1})	$\bar{\alpha}_f$ ($\times10^{-4}$) (K^{-1})	$\bar{\alpha}_{fs}$ ($\times10^{-4}$) (K^{-1})	—	—
400	2.4	7/5/20	−2.4/−1.6/−9.7	—	—

Downloaded 09/13/24 to 180.201.128.221. Redistribution subject to SEG license or copyright; see Terms of Use at http://library.seg.org/page/policies/terms
DOI:10.1190/geo2023-0625.1

$$\mathbf{k} = \boldsymbol{\kappa} + \mathrm{i}\boldsymbol{\alpha} = \kappa\hat{\boldsymbol{\kappa}} + \mathrm{i}\alpha\hat{\boldsymbol{\alpha}},$$
$$\mathbf{V}_{\mathrm{P}} = \frac{\omega}{\kappa}\hat{\boldsymbol{\kappa}}, \tag{13}$$

where the overhat defines a unit vector and $\boldsymbol{\alpha}$ is the attenuation vector.

R/T COEFFICIENTS AND AVO RESPONSE

Thermoporoelastic Zoeppritz equations

We consider a 2D thermo-poroelastic model with a plane interface, as in Hou et al. (2023a, Figure 1). For a wave incident obliquely at an angle θ_0, five reflected (P1, P2, T1, T2, and S) waves are present in the incidence medium ($z > 0$, upper-half space I) and five corresponding waves are in the transmission medium ($z < 0$, lower-half space II). The corresponding boundary conditions at the interface ($z = 0$) are

$$\mathbf{BC}^{\mathrm{I}} = \mathbf{BC}^{\mathrm{II}}, \tag{14}$$

where (Ignaczak and Ostoja-Starzewski, 2010; Wang et al., 2020)

$$\mathbf{BC}^{\bar{\imath}} = \left[u_z^{\bar{\imath}}, u_x^{\bar{\imath}}, \sigma_{zz}^{\bar{\imath}}, \sigma_{xz}^{\bar{\imath}}, w_z^{\bar{\imath}}, p^{\bar{\imath}}, T_s^{\bar{\imath}}, T_f^{\bar{\imath}}, \bar{\gamma}_s^{\bar{\imath}}\frac{\partial T_s^{\bar{\imath}}}{\partial z}, \bar{\gamma}_f^{\bar{\imath}}\frac{\partial T_f^{\bar{\imath}}}{\partial z}\right], \ \bar{\imath} = \mathrm{I}, \mathrm{II}. \tag{15}$$

The waves propagating in the thermoelastic medium are inhomogeneous, with inhomogeneity angle γ. The exact Zoeppritz equations are obtained with the boundary conditions (equation 14) considering generalized Snell's law and potential functions. We obtain

$$\mathbf{M} \cdot \mathbf{X} = \mathbf{N}, \tag{16}$$

whose derivation is given in Appendix B. Then, the exact R/T coefficients are

$$\mathbf{RT} = RT_\iota = X_\iota \frac{k_\iota}{k_0} = |RT_\iota| \exp(\mathrm{i}\vartheta_\iota),$$
$$\iota = 1, 2, \ldots, 10, \tag{17}$$

where X_ι denotes the ratio of the amplitude of the corresponding R/T wave to the incident wave; $\iota = 0$ represents the incident wave; $1, 2, \ldots, 5$ are the reflected P1, P2, T1, T2, and S waves, respectively, $6, 7, \ldots, 10$ are the corresponding transmitted waves, respectively; $|\cdot|$ represents the magnitude; and ϑ is the phase angle. The energy conservation at the interface verifies equation 17 (Hou et al., 2023a, equation 34).

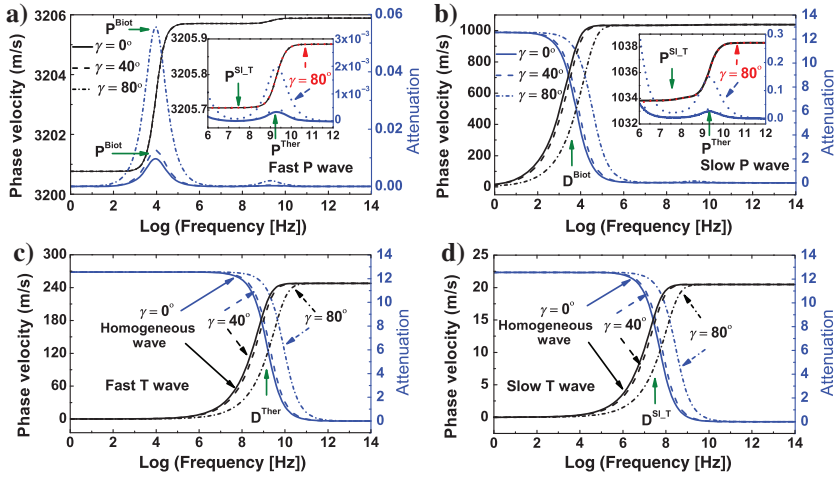

Figure 1. Phase velocities and attenuation factors of (a) fast P (P1), (b) slow P (P2), (c) fast T (T1), and (d) slow T (T2) waves as a function of frequency for water-saturated media (incidence medium I) with inhomogeneity angles 0° (solid lines), 40° (dashed lines), and 80° (dashed-dotted lines).

AVO approximation

Considering that the two half-spaces have similar characteristics, the Aki-Richards approximate formulas (Aki and Richards, 2002) are remarkably accurate (Zong et al., 2012; Hou et al., 2023b). Hence, due to the assumption of a small impedance contrast between the upper and lower mediums, we obtain

$$R_{\mathrm{PP1}} = \frac{1}{2}(\Delta_{\bar{\rho}} + \sec^2\theta_0 \Delta_{\bar{V}_{\mathrm{P1}}}) - 2\sin^2\theta_0 \left(\frac{\bar{V}_{\mathrm{S}}}{\bar{V}_{\mathrm{P1}}}\right)^2 (\Delta_{\bar{\rho}} - 2\Delta_{\bar{V}_{\mathrm{S}}}),$$
$$R_{\mathrm{PS}} = \frac{\sin\theta_0}{2\cos\theta_5}$$
$$\left[2\Delta_{\bar{V}_{\mathrm{S}}} - (2\Delta_{\bar{V}_{\mathrm{S}}} + \Delta_{\bar{\rho}})\left(\cos(2\theta_5) + \frac{2\bar{V}_{\mathrm{S}}}{\bar{V}_{\mathrm{P1}}}\cos\theta_0\cos\theta_5\right)\right],$$
$$T_{\mathrm{PP1}} = 1 - \Delta_{\bar{V}_{P1}} - \frac{1}{2}(\Delta_{\bar{\rho}} - \sec^2\theta_0 \Delta_{\bar{V}_{\mathrm{P1}}}),$$
$$T_{\mathrm{PS}} = \frac{\sin\theta_0}{2\cos\theta_5}$$
$$\left[2\Delta_{\bar{V}_{\mathrm{S}}} - (2\Delta_{\bar{V}_{\mathrm{S}}} + \Delta_{\bar{\rho}})\left(\cos(2\theta_5) - \frac{2\bar{V}_{\mathrm{S}}}{\bar{V}_{\mathrm{P1}}}\cos\theta_0\cos\theta_5\right)\right], \tag{18}$$

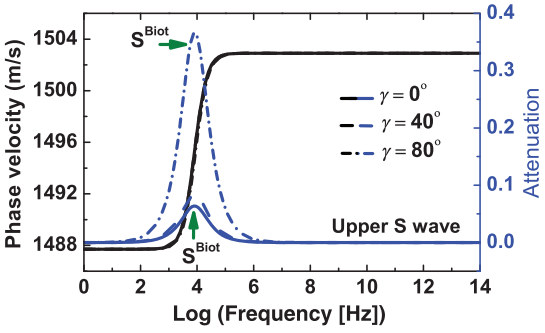

Figure 2. Same as Figure 1 but for the S wave.

Downloaded 09/13/24 to 180.201.128.221. Redistribution subject to SEG license or copyright; see Terms of Use at http://library.seg.org/page/policies/terms
DOI:10.1190/geo2023-0625.1

where $\Delta_{\hbar}$ is the ratio of the difference to the average of corresponding subscript parameters $\hbar$ in the two spaces and $\hbar$ represents V_{P1}, V_S, and ρ, respectively.

EXAMPLES

Let us assume the properties of the water/oil contacts in Table 1 (Pecker and Deresiewicz, 1973; Hou et al., 2023a; Liu et al., 2023). The relaxation times are $\tau_{1s/1f} = 0$, $\tau_{2s} = \tau_{3s} = 0.08$ ns, and $\tau_{2f} = \tau_{3f} = 2.5$ ns for water-saturated ($\tau_{2f} = \tau_{3f} = 1.6$ ns for oil-saturated) media, respectively, which coincide with the GL theory with $\tau_{3s/3f} = 0$, $\tau_{1s} = \tau_{2s} = 0.08$ ns, and $\tau_{1f} = \tau_{2f} = 2.5$ ns for water-saturated ($\tau_{1f} = \tau_{2f} = 1.6$ ns for oil-saturated) media.

Figures 1 and 2 show the dispersion and dissipation curves of four compressional waves and one shear wave, respectively, in a water-saturated medium, where the pronounced variation in the inhomogeneity angle can better illustrate its impact. The wave propagation here can simultaneously trigger macroscopic thermal flow and fluid flow. We found that the global Biot flow plays a leading role for the P1 and S waves, causing significant Biot attenuation peaks and consequent velocity dispersion (D^{Biot}) at approximately 10 kHz. Thus, at low frequencies, the inhomogeneity angle significantly affects the Biot peaks, as represented by the P^{Biot} and S^{Biot}. At high frequencies, thermal flow plays an important role and leads to thermal peaks for P1 and P2 waves, where the superscripts "Ther" and "Sl_T" denote the T1 and T2 effects, respectively. The inhomogeneity angle of the three slow compression waves (P2, T1, and T2) affects the corresponding frequency of dispersion. Considering the presence of heat waves in the fluid (T2 wave), the propagation of P2 is definitely affected by the thermal mechanism. In contrast, the dispersion of the S mode is hardly affected. The thermal effects mainly affect the attenuation and velocity dispersion of P1 and P2 waves, as shown in Figure 1. Unlike the P1 wave, the P2 and the T1 waves have different phase velocities but surprisingly the same attenuation rate at all frequencies, which may be caused by the different coupling patterns.

Figure 3 shows the phase velocities and attenuation of the P1 and P2 waves as functions of porosity and frequency in the oil-saturated media. The P1 wave has two relaxation peaks at approximately 10 kHz and 1 GHz, which are caused by the Biot effect and the thermal mechanism, respectively. The contribution of thermal fluid flow is the main factor producing the high-frequency attenuation peak at approximately 100 MHz. Higher porosity implies

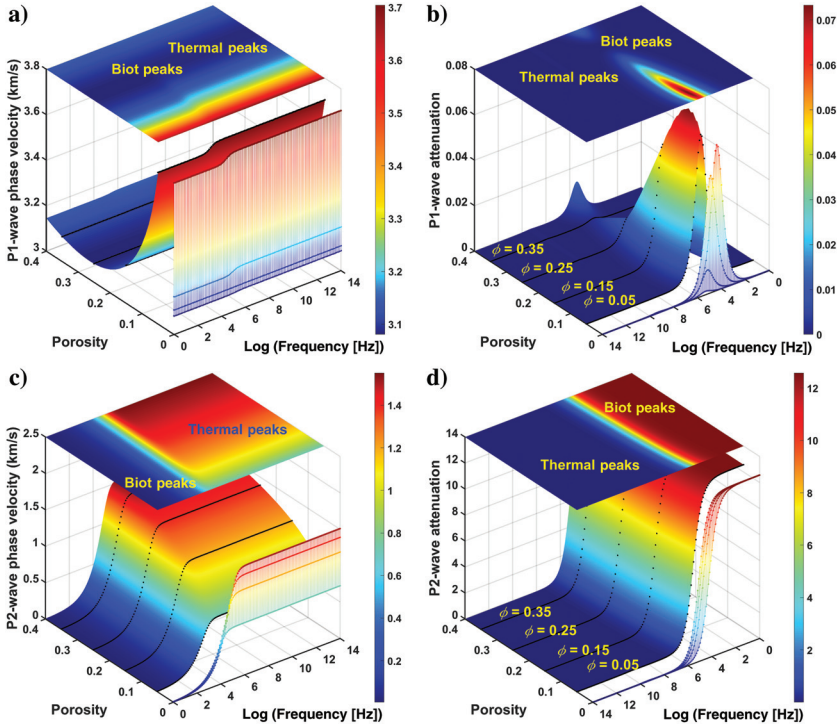

Figure 3. (a and c) Phase velocities and (b and d) attenuation factors of (a and b) fast P (P1) wave and (c and d) slow P (P2) wave as a function of frequency and porosity for oil-saturated media (transmission medium II), for a homogeneous wave.

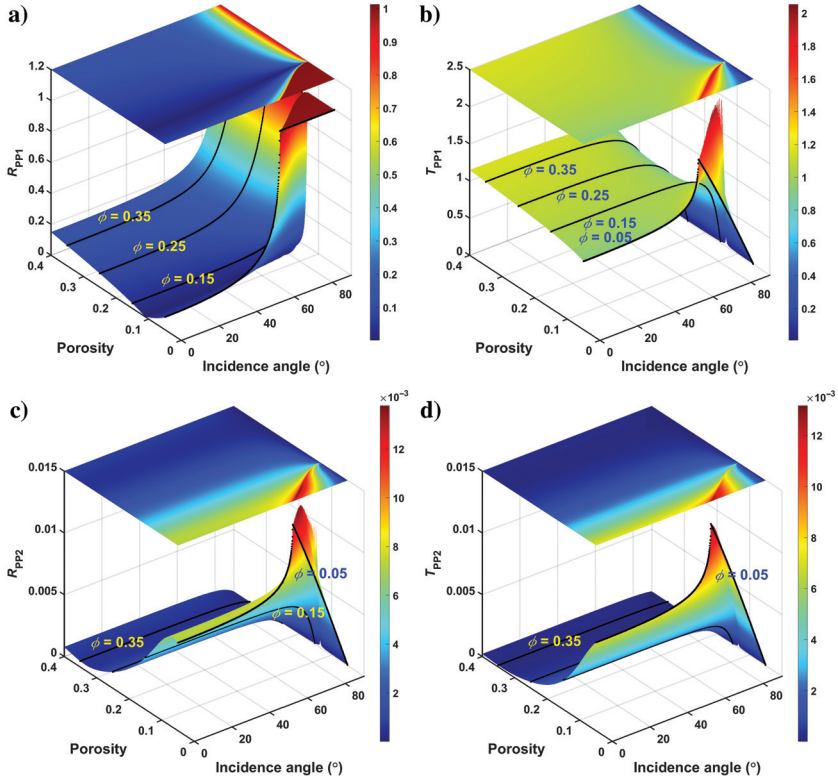

Figure 4. Reflected and transmitted fast P wave (a) R_{PP1}, (b) T_{PP1}, and slow P wave (c) R_{PP2} and (d) T_{PP2} amplitudes as a function of porosity and P-wave incidence angle at 50 Hz for the inhomogeneous cases.

Downloaded 09/13/24 to 180.201.128.221. Redistribution subject to SEG license or copyright; see Terms of Use at http://library.seg.org/page/policies/terms
DOI:10.1190/geo2023-0625.1

stronger solid-fluid coupling and lower composite density, resulting in a higher velocity of the P2 wave, whereas the opposite effect is observed for the P1 wave. The porosity dependence of the slow thermal peak of the first wave is not obvious. However, it is the main reason influencing the location of Biot's peak for the second wave.

Exact R/T coefficient

The effects of P-wave incidence angle and porosity on the R/T results are shown in Figures 4–6, taking into account the relatively low seismic frequency ($f = 50$ Hz). Because the exploration applications are primarily of interest for the P1 wave incidence, we focus on the observation of this incidence. We obtain the R/T coefficients calculated by equation 17, based on the properties provided in Table 1. Figures 4–6 show the variations in the R/T magnitudes of the P1, P2, T1, T2, and S waves as functions of the P-wave incidence angle and the porosity of the oil-saturated medium. The incidence velocity of the P wave is $V_{\mathrm{P1}} = 3200$ m/s from Figure 1, leading to significant porosity-dependent R/T coefficients. The results presented in Figures 4–6 show that the magnitudes have strong variations around the critical porosity ($\bar{\phi}^{\mathrm{II}} \approx 0.11$, with the same incidence and transmission P1 wave velocities). Below the critical porosity, the magnitudes of the reflected P1 waves increase with the oblique angles, reaching one at the critical angle, with the corresponding energy flux becoming zero until grazing incidence. Beyond this porosity, the critical angle disappears, as shown in Figure 4a. Accordingly, the transmitted P1 wave has a peak, as shown in Figure 4b. This is because the porosity decreases the velocity of the transmitted P1 wave (see Figure 3), and consequently the impedance contrast decreases up to the critical porosity at the same incidence and transmission velocities of the P1 wave. At the same time, as expected, the extremely slow velocities induce two T waves with relatively low R/T amplitudes (see Figure 1c and 1d). The P2 wave is induced by the pressure difference between the fluid and solid phases of the porous rock, whereas the temperature gradient causes the T1 wave. Despite the fact that the physical mechanisms are significantly different, the observed trends are similar, as depicted in Figures 4 and 5. The effects of porosity on the slow T wave are similar to those of the slow P wave, whereas the porosity dependence is more pronounced for the fast T wave. In contrast, the porosity-dependent behavior of S waves with high $\bar{\phi}^{\mathrm{II}}$ is more evident. In particular, the lower impedance of the P1$^{\mathrm{II}}$ wave caused by higher porosity increases the energy of the converted S waves, as shown in Figure 6. Meanwhile, the determination of energy ratios relies on the R/T coefficients (Hou et al., 2023a), and incidence angle and porosity will also impact the energy partitions. As depicted in Figure 7, the simulated vertical energy distribution primarily revolves around reflected and transmitted fast P and S waves as an example, due to the energy variation analogous with the corresponding R/T results (Figures 4–6), where energy fluxes mainly concentrate on the fast P waves, particularly under vertical incidence, with no generation of converted waves (Hou et al., 2022, 2023a).

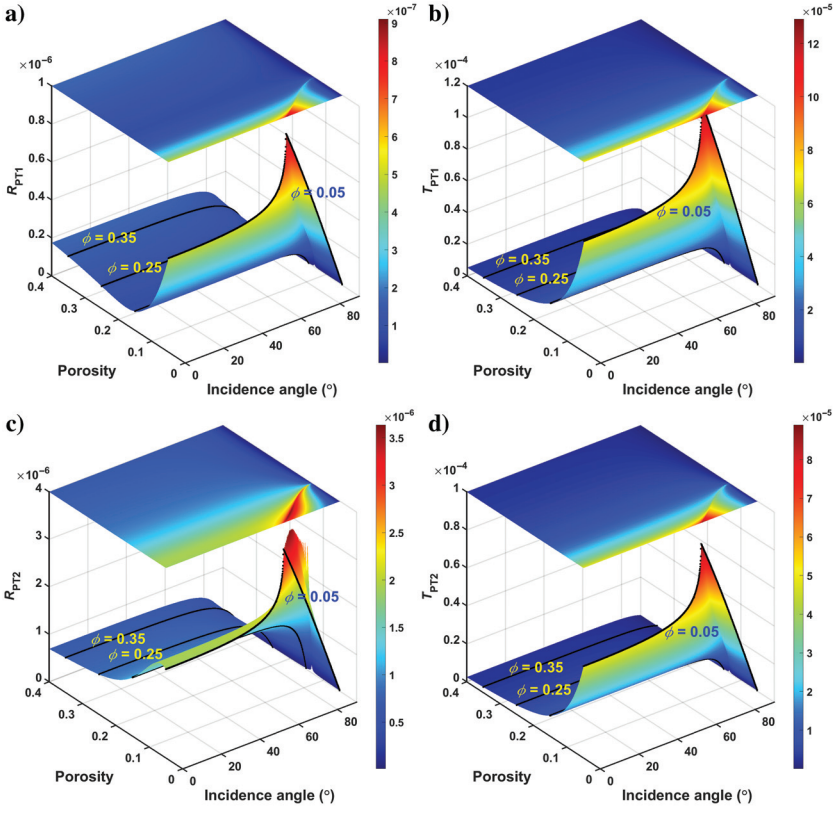

Figure 5. Reflected and transmitted fast T wave (a) R_{PT1}, (b) T_{PT1}, and slow T wave (c) R_{PT2} and (d) T_{PT2} amplitudes as a function of porosity and P-wave incidence angle at 50 Hz for homogeneous cases.

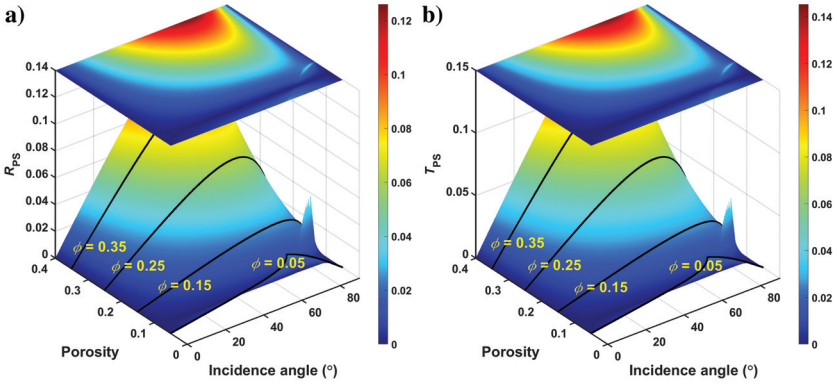

Figure 6. Reflected and transmitted S wave (a) R_{PS} and (b) T_{PS} amplitudes as a function of porosity and P-wave incidence angle at 50 Hz for homogeneous cases.

AVO response

We first compare the differences between the exact (labeled "Exact") and approximate (labeled

Downloaded 09/13/24 to 180.201.128.221. Redistribution subject to SEG license or copyright; see Terms of Use at http://library.seg.org/page/policies/terms
DOI:10.1190/geo2023-0625.1

"Pro") R/T magnitudes for the reflected and transmitted P1 and S waves, as shown in Figure 8. Thermoporelastic and Biot-poroelastic models are represented by "Ther" and "Biot," respectively, and we evaluated the models by the absolute value of the differences ($|\Delta|$) indicated by the red (TTG model), blue (ST model; Cheng et al., 2023) and black (Biot model) histogram errors. The errors illustrate the improvement of the thermoporelastic model compared with the Biot model. For the fast P wave, the calculation with the new thermoporelastic TTG model is also generally closer to the exact values, and the errors become negligible due to the assumption of a small angle of incidence. The approximation results of the S wave for the TTG and Biot models agree well, with the former model showing much better agreement, especially at small incidence angles, while the difference is much larger for the latter model.

A comparison with Biot's poroelastic theories has confirmed the accuracy of the developed approximate equation for thermoporoelasticity. To further investigate the practical applicability of the proposed model, we consider the corresponding synthetic seismogram of the fast P-wave displacement, as shown in Figure 9a. It is obtained by convolution of the Ricker wavelet, and the approximate results are shown in Figure 8a. It should be noted that Biot predicts stronger magnitudes for the petroleum reservoir at large incidence angles. We have shown that the proposed model significantly improves its accuracy for the approximate solution by introducing thermal properties to successfully extend the R/T coefficients. Moreover, variations of oil saturated and gas saturated in the lower media are used to compare the AVO responses for the thermoporoelastic model, as shown in Figure 9b, processed

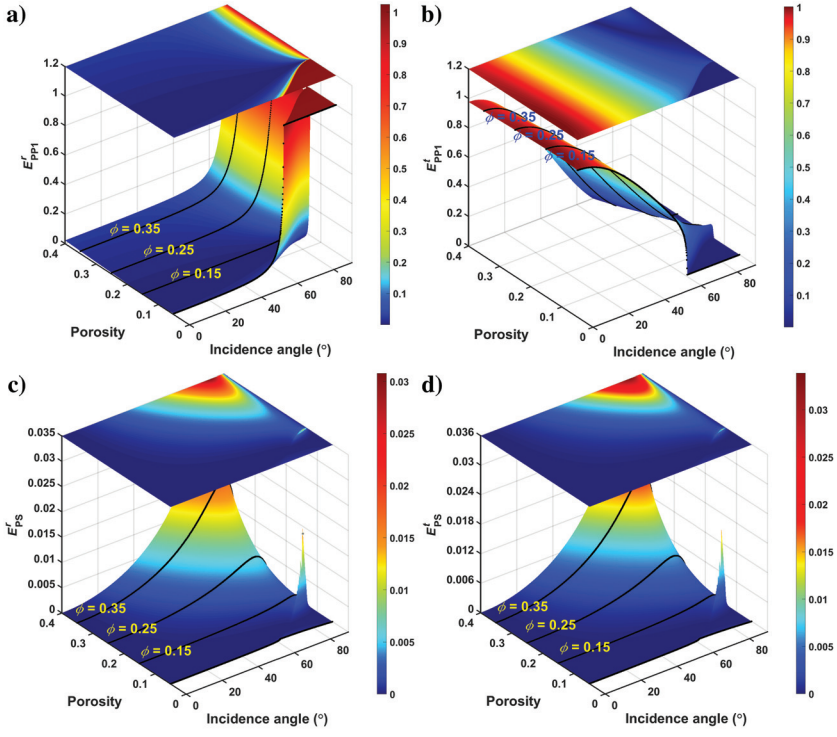

Figure 7. Reflected and transmitted fast P wave (a) E^r_{PP1}, (b) E^t_{PP1}, and S wave (c) E^r_{PS} and (d) E^t_{PS} energy ratios as a function of porosity and P-wave incidence angle at 50 Hz for homogeneous cases.

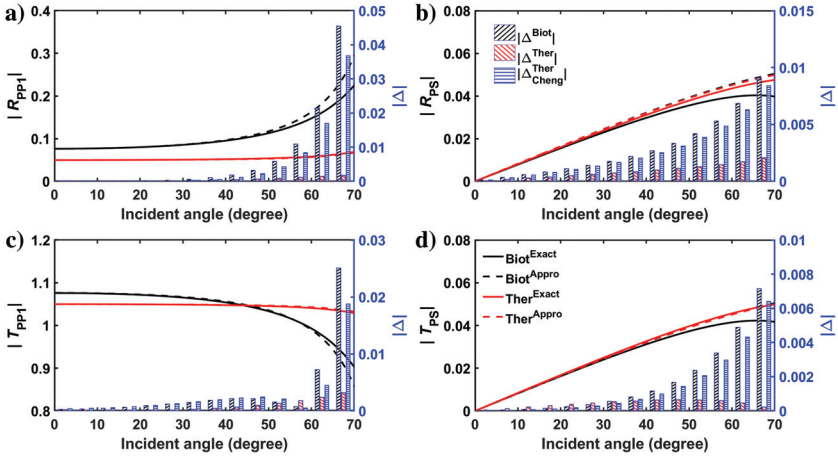

Figure 8. Reflection coefficients of (a) fast P and (b) S waves, transmission coefficients of (c) fast P and (d) S waves, and the difference (bar chart) between the exact and AVO approximate solutions at 50 Hz, corresponding to the Biot poroelastic (black), ST thermoporoelastic (blue) and TT thermoporoelastic (red) theories.

Downloaded 09/13/24 to 180.201.128.221. Redistribution subject to SEG license or copyright; see Terms of Use at http://library.seg.org/page/policies/terms
DOI:10.1190/geo2023-0625.1

Table 2. Properties of the CO_2 reservoir.

K_m (GPa)	K_f (GPa)	μ (GPa)	ρ_f (g/cm^3)	$\bar{\phi}$	T_0 (K)
8.5	0.025	7.0	0.33	0.27	335.4
β_f ($\times 10^6$)	$\bar{\gamma}_f^*$	$\bar{\tilde{\alpha}}_f$ ($\times 10^{-3}$)	$\bar{\tilde{\alpha}}_{fs}$ ($\times 10^{-4}$)	η_f ($\times 10^{-4}$)	τ_{2f}
kg/(m · s^2 · K)	m · kg/(s^3 · K)	K^{-1}	K^{-1}	Pa s	ns
2	2	6	−4.7	0.2	3.2

in the same way as Figure 9a. When there are saturated pores in the transmission medium, the gas-saturated case shows lower responses. Because the AVO response is affected by the type of saturated fluid, it can serve as a potential method to discriminate the fluid.

We apply the proposed model to the CO_2 geosequestration reservoir of the CRC-3 injection well as part of the CO2CRC Otway Project in Victoria, Australia (Caspari et al., 2015). According to Pevzner et al. (2022), the estimated thickness of the CO_2 plume is 11 m and the corresponding properties are provided in Table 2 (same values as in Table 1, not provided), where the overlying formation is water saturated and has the characteristics of Table 1 except T_0 = 330 K. In addition, the solid properties of the underlying (below CO_2 reservoirs) are the same as those of the CO_2 reservoir (Table 2) but water-saturated (Table 1) and $\phi = 0.1$. The proposed approximate thermoporoelastic method demonstrates the ability to identify thin reservoirs, particularly evident for larger offsets, as shown in Figure 10.

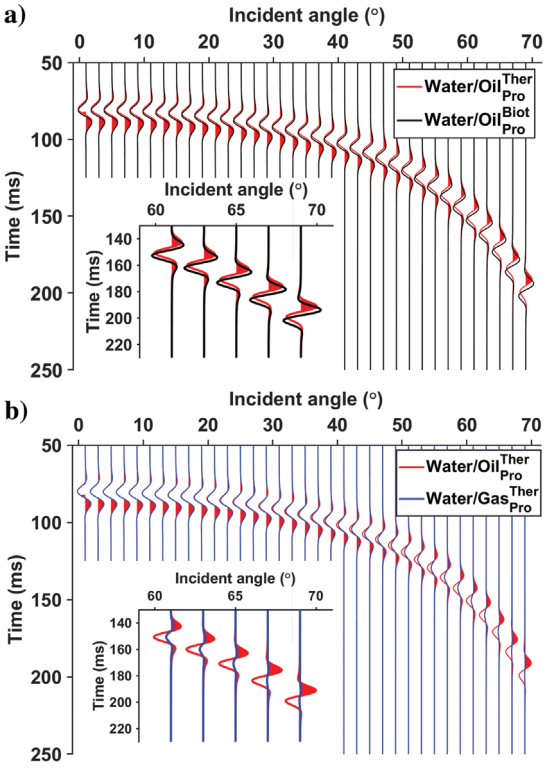

Figure 9. Synthetic seismograms for (a) thermoporoelastic (red lines) and Biot (black lines) models of water-saturated/oil-saturated interface, (b) thermoporoelastic interfaces of the water-saturated/oil-saturated (red lines) and water-saturated/gas-saturated (blue lines) media based on the AVO approximate equations.

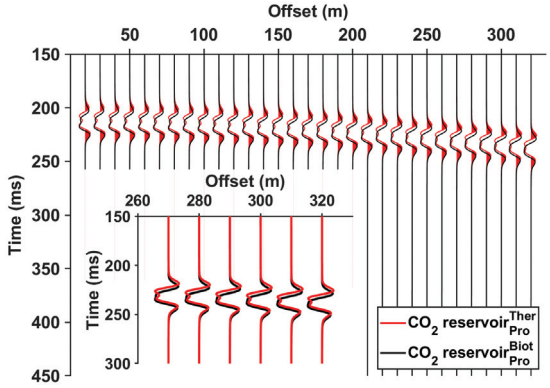

Figure 10. Synthetic seismograms of CO_2 geosequestration reservoir thermoporoelastic (red lines) and Biot (black lines) models based on the AVO approximate equations.

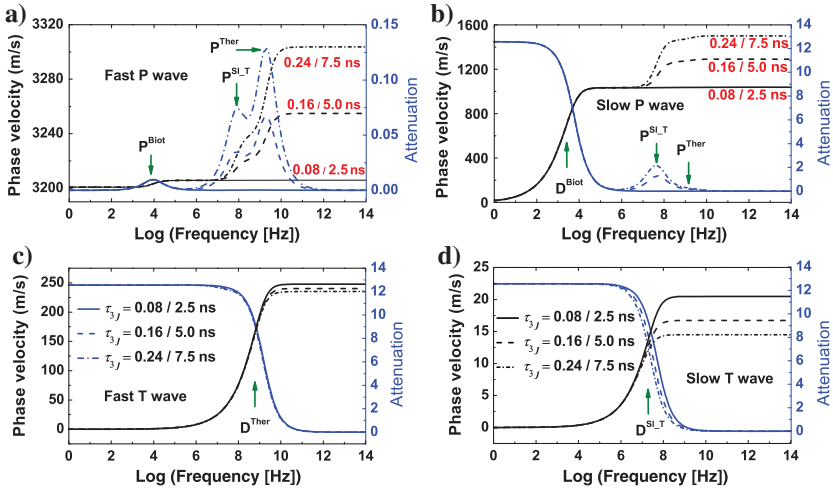

Figure 11. Phase velocities (black lines) and attenuation factors (blue lines) of four compressional waves as a function of frequency calculated with the GLS theory. The inhomogeneity angle is 0° (homogeneous waves), whereas the relaxation times provided in Table 1 are multiplied by $\tau_{3s}/\tau_{3f} = 0.16/5.0$ ns (dashed lines) and $\tau_{3s}/\tau_{3f} = 0.24/7.5$ ns (dashed-dotted lines), respectively.

Downloaded 09/13/24 to 180.201.128.221. Redistribution subject to SEG license or copyright; see Terms of Use at http://library.seg.org/page/policies/terms
DOI:10.1190/geo2023-0625.1

Attenuation effects in the context of GLS theory

In this section, we further investigate the effects of relaxation times on frequency-dependent dispersion and dissipation. Consider the GL model assuming different values of τ_{1j} ($j = s, f$), consistent with the GLS theory for $\tau_{3j}^{\mathrm{GLS}} = \tau_{1j}^{\mathrm{GL}}$ (Ignaczak and Ostoja-Starzewski, 2010; Wang et al., 2021). The combined effects of the models on phase velocities and attenuation factors of compressional waves are shown in Figure 11. The high-frequency sensitivity of the two thermal peaks of the P1 wave systematically increases, especially for the thermal peak, while the slow thermal peak of the P2 wave is more sensitive. The increased attenuation leads to stronger dispersion, as shown in Figure 11a and 11b. Unlike the inhomogeneity angle, the different relaxation times imply various thermal-balance processes, and therefore the relaxation times affect not only the attenuation but also the phase velocities. Moreover, the LS and GL models have consistent frequency dependence in the range of the Biot attenuation.

CONCLUSION

We have derived the R/T coefficients of a plane wave with the inhomogeneity angle γ incident on the interface separating two half-spaces based on the TTG thermoporoelastic LS and GL equations. The coefficients as a function of incidence angle and porosity are presented. We have also developed the corresponding AVO approximation to compare with that of the Biot poroelastic model and to study the effects of fluids. The approximation allows the application of equations with thermal properties in a simplified way.

The inhomogeneity angle γ is found to affect the attenuation values of the P1 and S waves more strongly, with an increase in γ leading to enhanced attenuation, especially in the range caused by Biot dispersion, while the dispersion for the other three waves shifts to the high frequencies. Though the observable attenuations of P2 and T1 waves are identical, the differences in the physical processes of the two cases cause the distinctive phase velocity dispersion. In addition, the velocity dispersion is affected by the small variation in thermal relaxation times, especially at high frequencies and for P1 waves, which indicates the significance of thermal effects.

The porosity- and frequency-dependent R/T behavior in the seismic band is based on the exact Zoeppritz equations. The critical angle of P1 waves increases with porosity ($\bar{\phi}$) until it vanishes ($\bar{\phi} \approx 0.11$), whereas the velocity of the P1 wave in the transmission medium is equal to the velocity in the incidence.

Moreover, we proposed a TTG thermoporoelastic approximation to simplify the exact calculations. Comparisons with Biot and the approximation show that the simplified results agree satisfactorily with the exact values and are better than those predicted by the Biot model. The differences between water/gas saturated and water/oil saturated show the effects of different reservoirs on the AVO response and help to distinguish hydrocarbon fill, which leads to a more successful interpretation in seismic exploration. Data from a real CO_2 geosequestration reservoir used to construct a model illustrates that the proposed AVO approximation can significantly enhance the ability to distinguish thin reservoirs.

ACKNOWLEDGMENTS

This work was supported in part by the National Natural Science Foundation of China under grant 42230803 and 41821002 and in part by the 111 Project "Deep-Superdeep Oil and Gas Geophysical Exploration" under grant B18055.

DATA AND MATERIALS AVAILABILITY

Data associated with this research are available and can be obtained by contacting the corresponding author.

APPENDIX A

EXPRESSIONS for A AND INHOMOGENEITY ANGLE

In the equation 10, the corresponding parameters are

$$
\begin{aligned}
a_{61} &= -\omega M(2\bar{\alpha}\rho_f - \rho) + E_G(\mathrm{i}b + m\omega),\\
a_{62} &= F_{11}\bar{\tau}_{s2}\bar{\gamma}_f + F_{22}\bar{\gamma}_s\bar{\tau}_{f2},\\
a_{63} &= F_{12}F_{21} - F_{11}F_{22},\\
a_{64} &= R_{21}^2\bar{\gamma}_f\bar{\tau}_{s1}\bar{\tau}_{s3} + R_{22}^2\bar{\gamma}_s\bar{\tau}_{f1}\bar{\tau}_{f3},\\
a_{65} &= R_{11}\bar{\gamma}_f\bar{\tau}_{s1}\bar{\tau}_{s3}(R_{11} - 2\bar{\alpha}R_{21}),\\
a_{66} &= R_{12}\bar{\gamma}_s\bar{\tau}_{f1}\bar{\tau}_{f3}(R_{12} - 2\bar{\alpha}R_{22}),\\
a_{41} &= F_{21}R_{21} - F_{11}R_{22},\\
a_{42} &= F_{12}R_{22} - F_{22}R_{21},\\
a_{43} &= \omega\rho_f^2 - (m\omega + \mathrm{i}b)\rho,\\
a_{44} &= -\bar{\tau}_{f1}\bar{\tau}_{f3}\bar{\tau}_{s1}\bar{\tau}_{s3}T_0^2(R_{11}R_{22} - R_{12}R_{21})^2,\\
a_{45} &= \bar{\tau}_{f1}\bar{\tau}_{f3}\{R_{22}^2(-E_G\bar{\tau}_{s2}F_{11} - \omega\rho\bar{\gamma}_s) + 2R_{22}R_{12}(M\bar{\alpha}F_{11}\tau_{s2}\\
&\quad + \omega\bar{\gamma}_s\rho_f) - R_{12}^2[MF_{11}\bar{\tau}_{s2} + \bar{\gamma}_s(m\omega + \mathrm{i}b)]\},\\
a_{46} &= \bar{\tau}_{s1}\bar{\tau}_{s3}\{R_{21}^2(-E_G\bar{\tau}_{f2}F_{22} - \omega\rho\bar{\gamma}_f) + 2R_{21}R_{11}(M\bar{\alpha}F_{22}\tau_{f2}\\
&\quad + \omega\bar{\gamma}_f\rho_f) - R_{11}^2[MF_{22}\bar{\tau}_{f2} + \bar{\gamma}_f(m\omega + \mathrm{i}b)]\},\\
a_{47} &= \bar{\tau}_{s3}\bar{\tau}_{f1}\bar{\tau}_{f2}F_{21}\{[(-\bar{\alpha}R_{22} + R_{12})R_{11} - R_{12}R_{21}\bar{\alpha}]M\\
&\quad + R_{21}R_{22}E_G\},\\
a_{48} &= \bar{\tau}_{f3}\bar{\tau}_{s1}\bar{\tau}_{s2}F_{12}\{[(-\bar{\alpha}R_{22} + R_{12})R_{11} - R_{12}R_{21}\bar{\alpha}]M\\
&\quad + R_{21}R_{22}E_G\},\\
a_{21} &= (R_{11}R_{22} + R_{12}R_{21})\rho_f - R_{21}R_{22}\rho,\\
a_{22} &= \bar{\tau}_{s3}\bar{\tau}_{f2}[F_{22}R_{21}\bar{\tau}_{s1}(R_{21}\rho - 2R_{11}\rho_f) + a_{21}F_{21}\bar{\tau}_{f1}],\\
a_{23} &= \bar{\tau}_{s2}\bar{\tau}_{f3}[F_{11}R_{22}\bar{\tau}_{f1}(R_{22}\rho - 2R_{12}\rho_f) + a_{21}F_{12}\bar{\tau}_{s1}],\\
a_{24} &= \bar{\tau}_{s3}\bar{\tau}_{f2}R_{11}(F_{21}R_{12}\bar{\tau}_{f1} - R_{11}\bar{\tau}_{s1}F_{22}),\\
a_{25} &= \bar{\tau}_{f3}\bar{\tau}_{s2}R_{12}(F_{11}R_{12}\bar{\tau}_{f1} - R_{11}\bar{\tau}_{s1}F_{12}),\\
a_{26} &= \bar{\tau}_{f2}\bar{\tau}_{s2}a_{63} + \omega a_{43}a_{62}.
\end{aligned}
\tag{A-1}
$$

For solving for κ and α, we obtain (Hou et al., 2022)

$$
\begin{aligned}
\kappa^2 &= \sqrt{\left[\frac{\mathrm{Re}(k^2)}{2}\right]^2 + \left[\frac{\mathrm{Im}(k^2)}{2\cos\gamma}\right]^2} + \frac{\mathrm{Re}(k^2)}{2},\\
\alpha^2 &= \sqrt{\left[\frac{\mathrm{Re}(k^2)}{2}\right]^2 + \left[\frac{\mathrm{Im}(k^2)}{2\cos\gamma}\right]^2} - \frac{\mathrm{Re}(k^2)}{2},
\end{aligned}
\tag{A-2}
$$

where k corresponds to the P wave (k_{P}) and S wave (k_{S}) complex wavenumbers.

Downloaded 09/13/24 to 180.201.128.221. Redistribution subject to SEG license or copyright; see Terms of Use at http://library.seg.org/page/policies/terms
DOI:10.1190/geo2023-0625.1

APPENDIX B

COMPONENTS OF MATRICES M AND N

Similar to Hou et al. (2023a, equation 21) the potential functions in incidence media correspond to $m = 1$, $n = 4$, and $b = 5$, and $m = 6$, $n = 9$, and $b = 10$ for transmission media. Substituting the potential functions into the boundary conditions (equation 14), we obtain equation 17, in which the expressions of $\mathbf{M}$ are as follows:

$$
\begin{cases}
M_{1a}=q_a, M_{2a}=p_a,\\
M_{3a}=-(p_a^2+q_a^2)[\lambda^{\mathrm{I}}+M^{\mathrm{I}}\bar{\alpha}^{\mathrm{I}}(\nu_a+\bar{\alpha}^{\mathrm{I}})]-2\mu^{\mathrm{I}}q_a^2+\mathrm{i}(R_{11}^{\mathrm{I}}\delta_a\bar{\tau}_{s1}^{\mathrm{I}}+R_{12}^{\mathrm{I}}\chi_a\bar{\tau}_{f1}^{\mathrm{I}}),\\
M_{4a}=2\mu^{\mathrm{I}}p_aq_a,\ M_{5a}=q_a\nu_a,\\
M_{6a}=M^{\mathrm{I}}(p_a^2+q_a^2)(\nu_a+\bar{\alpha}^{\mathrm{I}})-\mathrm{i}\frac{R_{12}^{\mathrm{I}}\chi_a}{\bar{\alpha}^{\mathrm{I}}}\bar{\tau}_{f1}^{\mathrm{I}},\\
M_{7a}=\delta_a,\ M_{8a}=\bar{\gamma}_s^{\mathrm{I}}\delta_aq_a,\ M_{9a}=\chi_a,\ M_{(10)a}=\bar{\gamma}_f^{\mathrm{I}}\chi_aq_a,\ (a=1,2,3,4),\\
M_{1b}=q_b,\ M_{2b}=-p_b,\\
M_{3b}=(p_b^2+q_b^2)[\lambda^{\mathrm{II}}+M^{\mathrm{II}}\bar{\alpha}^{\mathrm{II}}(\nu_a+\bar{\alpha}^{\mathrm{II}})]+2\mu^{\mathrm{II}}q_b^2-\mathrm{i}(R_{11}^{\mathrm{II}}\delta_a\bar{\tau}_{s1}^{\mathrm{II}}+R_{12}^{\mathrm{II}}\chi_a\bar{\tau}_{f1}^{\mathrm{II}}),\\
M_{4b}=2\mu^{\mathrm{II}}p_bq_b,\ M_{5b}=q_b\nu_b,\\
M_{6b}=-M^{\mathrm{II}}(p_b^2+q_b^2)(\nu_b+\bar{\alpha}^{\mathrm{II}})+\mathrm{i}\frac{R_{12}^{\mathrm{II}}\chi_b}{\bar{\alpha}^{\mathrm{II}}}\bar{\tau}_{f1}^{\mathrm{II}},\\
M_{7b}=-\delta_b,\ M_{8b}=\bar{\gamma}_s^{\mathrm{II}}\delta_bq_b,\ M_{9b}=-\nu_b,\ M_{(10)b}=\bar{\gamma}_f^{\mathrm{II}}\nu_bq_b,\ (b=6,7,8,9),\\
M_{15}=p_5,\ M_{1(10)}=-p_{(10)},\ M_{25}=-q_5,\ M_{2(10)}=-q_{(10)},\\
M_{35}=-2\mu^{\mathrm{I}}p_5q_5,\ M_{3(10)}=-2\mu^{\mathrm{II}}p_{(10)}q_{(10)},\\
M_{45}=\mu^{\mathrm{I}}(p_5^2-q_5^2),\ M_{4(10)}=-\mu^{\mathrm{II}}(p_{(10)}^2-q_{(10)}^2),\\
M_{55}=p_5\nu_5,\ M_{5(10)}=-p_{(10)}\nu_{(10)},\ M_{c5}=M_{c10}=0,\ (c=6,7,\ldots,10),
\end{cases}
\tag{B-1}
$$

and the expressions of $\mathbf{N}$ are

$$
\begin{cases}
N_1=\Xi q_0-(1-\Xi)p_0,\quad N_2=-\Xi p_0-(1-\Xi)q_0,\\
N_3=\Xi\{(p_0^2+q_0^2)[\lambda^{\mathrm{I}}+M^{\mathrm{I}}\bar{\alpha}^{\mathrm{I}}(\nu_a+\bar{\alpha}^{\mathrm{I}})]\\
+2\mu^{\mathrm{I}}q_0^2-\mathrm{i}(R_{11}^{\mathrm{I}}\delta_a\bar{\tau}_{s1}^{\mathrm{I}}+R_{12}^{\mathrm{I}}\chi_a\bar{\tau}_{f1}^{\mathrm{I}})\}-2\mu^{\mathrm{I}}p_0q_0(1-\Xi),\\
N_4=2\mu^{\mathrm{I}}p_0q_0\Xi-\mu^{\mathrm{I}}(p_0^2-q_0^2)(1-\Xi),\\
N_5=\Xi q_0\nu_0-p_0\nu_0(1-\Xi),\\
N_6=\Xi\left(-M^{\mathrm{I}}(p_0^2+q_0^2)(\nu_0+\bar{\alpha}^{\mathrm{I}})+\mathrm{i}\frac{R_{12}^{\mathrm{I}}\chi_a}{\bar{\alpha}^{\mathrm{I}}}\bar{\tau}_{f1}^{\mathrm{I}}\right),\\
N_7=-\Xi\delta_0,\quad N_8=\bar{\gamma}_s^{\mathrm{I}}\delta_0q_0\Xi,\\
N_9=-\Xi\nu_0,\quad N_{10}=\bar{\gamma}_f^{\mathrm{I}}\nu_0q_0\Xi,
\end{cases}
\tag{B-2}
$$

where

$$
\begin{aligned}
&\xi_{\iota 1}=\omega^2\rho_f-M\bar{\alpha}k_\iota^2,\ \xi_{\iota 2}=\omega^2\rho-E_Gk_\iota^2,\ \xi_{\iota 3}=\mathrm{i}b\omega+m\omega^2-Mk_\iota^2,\\
&\xi_{\iota 4}=-T_0\omega\bar{\tau}_{s3}k_\iota^2,\ \xi_{\iota 5}=\omega\bar{\tau}_{s2}F_{11}-\bar{\gamma}_sk_\iota^2,\\
&\xi=\bar{\tau}_{f1}[\xi_{\iota 4}R_{21}\bar{\tau}_{s1}(R_{11}R_{22}-R_{12}R_{21})+\mathrm{i}\xi_{\iota 5}(\xi_{\iota 1}R_{22}-\xi_{\iota 3}R_{12})]\\
&-\mathrm{i}\omega\bar{\tau}_{s1}\bar{\tau}_{s2}F_{12}(\xi_{\iota 1}R_{21}-\xi_{\iota 3}R_{11}),\\
&\xi_\nu=-\bar{\tau}_{f1}[\xi_{\iota 4}R_{11}\bar{\tau}_{s1}(R_{11}R_{22}-R_{12}R_{21})+\mathrm{i}\xi_{\iota 5}(\xi_{\iota 2}R_{22}-\xi_{\iota 1}R_{12})]\\
&-\mathrm{i}\omega\bar{\tau}_{s1}\bar{\tau}_{s2}F_{12}(\xi_{\iota 1}R_{11}-\xi_{\iota 2}R_{21}),\\
&\xi_\delta=-\mathrm{i}\bar{\tau}_{f1}\xi_{\iota 4}[\xi_{\iota 1}(R_{11}R_{22}+R_{12}R_{21})-\xi_{\iota 2}R_{21}R_{22}-\xi_{\iota 3}R_{11}R_{12}]\\
&+\omega\bar{\tau}_{s2}F_{12}(\xi_1^2-\xi_{\iota 2}\xi_{\iota 3}),\\
&\xi_\chi=\mathrm{i}\bar{\tau}_{s1}\xi_{\iota 4}(2\xi_{\iota 1}R_{11}R_{21}-\xi_{\iota 3}R_{11}^2-\xi_{\iota 2}R_{21}^2)-\xi_{\iota 5}(\xi_{\iota 1}^2-\xi_{\iota 2}\xi_{\iota 3}),\\
&\nu_\iota=\frac{\xi_\nu}{\xi},\ \delta_\iota=\frac{\xi_\delta}{\xi},\ \chi_\iota=\frac{\xi_\chi}{\xi},\ \iota=0,1,\ldots,9\ \text{and}\neq 5.\\
&\nu_\iota=\frac{-\omega\rho_f}{m\omega+\mathrm{i}\eta/\bar{\kappa}},\ \iota=5,10.
\end{aligned}
\tag{B-3}
$$

The horizontal (p_ι) and vertical wavenumbers (q_ι), obtained from the complex wavenumbers (k_ι) are

$$
\begin{aligned}
&q_\iota=D_R+\mathrm{i}D_I,\quad D=\pm\mathrm{pv}\sqrt{k_\iota^2-p_\iota^2},\\
&p_\iota=|\kappa_\iota|\sin\theta_\iota-\mathrm{i}|\alpha_\iota|\sin(\theta_\iota-\gamma_\iota),\quad \mathrm{i}=0,1,\ldots,10,
\end{aligned}
\tag{B-4}
$$

where "pv" denotes the principal value and p_ι remain unchanged during the propagation, following the generalized Snell's law (Carcione, 2022). The downward waves correspond to the minus signs; otherwise, the positive sign holds.

REFERENCES

Aki, K., and P. G. Richards, 2002, Quantitative seismology, 2nd ed.: University Science Books.

Anderson, D. L., 1989, Theory of the earth: Blackwell Scientific Publications.

Biot, M. A., 1956a, Thermoelasticity and irreversible thermodynamics: Journal of Applied Physics, **27**, 240–253, doi: 10.1063/1.1722351.

Biot, M. A., 1956b, The theory of propagation of elastic waves in a fluid-saturated porous solid, I. Low-frequency range II. Higher frequency range: The Journal of the Acoustical Society of America, **28**, 168–178, doi: 10.1121/1.1908239.

Biot, M. A., 1962, Mechanics of deformation and acoustic propagation in porous media: Journal of Applied Physics, **33**, 1482–1498, doi: 10.1063/1.1728759.

Carcione, J. M., 2022, Wave fields in real media. Theory and numerical simulation of wave propagation in anisotropic, anelastic, porous and electromagnetic media, 4th ed. : Elsevier.

Carcione, J. M., F. Cavallini, E. Wang, J. Ba, and L. Y. Fu, 2019, Physics and simulation of wave propagation in linear thermoporoelastic media: Journal of Geophysical Research: Solid Earth, **124**, 8147–8166, doi: 10.1029/2019JB017851.

Caspari, E., R. Pevzner, B. Gurevich, T. Dance, J. Ennis-King, Y. Cinar, and M. Lebedev, 2015, Feasibility of CO_2 plume detection using 4D seismic: CO2CRC Otway Project case study — Part 1: Rock-physics modeling: Geophysics, **80**, no. 4, B95–B104, doi: 10.1190/geo2014-0459.1.

Chandrasekharaiah, D. S., 1998, Hyperbolic thermoelasticity: A review of recent literature: ASME Journal of Applied Mechanics Reviews, **51**, 705–729, doi: 10.1115/1.3098984.

Cheng, Y., L. Y. Fu, W. Hou, J. M. Carcione, W. Deng, and Z. Wang, 2023, Thermoporoelastic AVO modeling of Olkaria geothermal reservoirs: TechRxiv, Preprint.

De La Cruz, V., P. N. Sahay, and T. J. T. Spanos, 1993, Thermodynamics of porous media: Proceedings of the Royal Society of London. Series A: Mathematical and Physical Sciences, **443**, 247–255, doi: 10.1098/rspa.1993.0143.

De La Cruz, V., and T. J. T. Spanos, 1989, Thermomechanical coupling during seismic wave propagation in a porous medium: Journal of Geophysical Research: Solid Earth, **94**, 637–642, doi: 10.1029/JB094iB01p00637.

Dhaliwal, R. S., and H. H. Sherief, 1980, Generalized thermoelasticity for anisotropic media: Quarterly of Applied Mathematics, **38**, 1–8, doi: 10.1090/qam/575828.

Green, A. E., and K. A. Lindsay, 1972, Thermoelasticity: Journal of Elasticity, **2**, 1–7, doi: 10.1007/BF00045689.

Hou, W., L. Y. Fu, and J. M. Carcione, 2023a, Reflection and transmission of inhomogeneous plane waves in thermoporoelastic media: Surveys in Geophysics, **44**, 1897–1917, doi: 10.1007/s10712-023-09782-z.

Hou, W., L. Y. Fu, and J. M. Carcione, 2023b, Amplitude-variation-with-offset approximation in thermoelastic media: Geophysics, **88**, no. 1, MR25–MR33, doi: 10.1190/geo2021-0815.1.

Hou, W., L. Y. Fu, J. M. Carcione, and T. Han, 2022, Reflection and transmission of inhomogeneous plane waves in thermoelastic media: Frontiers in Earth Science, **10**, 1–16, doi: 10.3389/feart.2022.850331.

Hou, W., L. Y. Fu, J. Wei, and Z. Wang, 2021, Characteristics of wave propagation in thermoelastic medium: Chinese Journal of Geophysics, **64**, 1364–1374, doi: 10.6038/cjg2021N0458.

Ignaczak, J., and M. Ostoja-Starzewski, 2010, Thermoelasticity with finite wave speeds: Oxford University Press.

Kumar, M., J. Bhagwan, P. Kaswan, X. Liu, and M. Kumari, 2023, Inhomogeneous waves propagation in double-porosity thermoelastic media: International Journal of Numerical Methods for Heat & Fluid Flow, **33**, 2927–2962, doi: 10.1108/HFF-03-2023-0146.

Kumar, M., X. Liu, K. K. Kalkal, V. Dalal, and M. Kumari, 2022b, Inhomogeneous wave reflection from the surface of a partially saturated

thermoelastic porous media: International Journal of Numerical Methods for Heat & Fluid Flow, **32**, 1911–1943, doi: 10.1108/HFF-04-2021-0279.
Kumar, M., X. Liu, M. Kumari, and P. Yadav, 2022a, Wave propagation at the welded interface of an elastic solid and unsaturated poro-thermoelastic solid: International Journal of Numerical Methods for Heat & Fluid Flow, **32**, 3526–3550, doi: 10.1108/HFF-01-2022-0008.
Kumari, M., P. Kaswan, M. Kumar, and P. Yadav, 2022, Reflection of inhomogeneous plane waves at the surface of an unsaturated porothermoelastic media: The European Physical Journal Plus, **137**, 729, doi: 10.1140/epjp/s13360-022-02880-8.
Landau, L. D., and E. M. Lifshitz, 1986, Theory of elasticity, 3rd ed., volume **7**: Elsevier.
Liu, H., G. Dai, F. Zhou, and X. Cao, 2022, A mixture theory analysis for reflection phenomenon of homogeneous plane-P1-wave at the boundary of unsaturated porothermoelastic media: Geophysical Journal International, **228**, 1237–1259, doi: 10.1093/gji/ggab379.
Liu, H., G. Dai, F. Zhou, and Z. Mu, 2021, Propagation behavior of homogeneous plane-P1-wave at the interface between a thermoelastic solid medium and an unsaturated porothermoelastic medium: The European Physical Journal Plus, **136**, 1–27, doi: 10.1140/epjp/s13360-020-01001-7.
Liu, Y., L. Y. Fu, W. Deng, W. Hou, J. M. Carcione, and J. Wei, 2023, Simulation of wave propagation in thermoporoelastic media with dual-phase-lag heat conduction: Journal of Thermal Stresses, **46**, 620–638, doi: 10.1080/01495739.2023.2193225.
Lord, H. W., and Y. Shulman, 1967, A generalized dynamical theory of thermoelasticity: Journal of the Mechanics and Physics of Solids, **15**, 299–309, doi: 10.1016/0022-5096(67)90024-5.
Nield, D. A., and A. Bejan, 2006, Convection in porous media, 3rd ed.: Springer.
Noda, N., 1990, Thermal stress problem in a fluid-filled porous circular cylinder: Zeitschrift fur Angewandte Mathematik und Mechanik, **70**, 543–549, doi: 10.1002/zamm.19900701203.
Pecker, C., and H. Deresiewicz, 1973, Thermal effects on wave propagation in liquid-filled porous media: Acta Mechanica, **16**, 45–64, doi: 10.1007/BF01177125.
Pevzner, R., S. Glubokovskikh, R. Isaenkov, P. Shashkin, K. Tertyshnikov, S. Yavuz, B. Gurevich, J. Correa, T. Wood, and B. Freifeld, 2022, Monitoring subsurface changes by tracking direct-wave amplitudes and traveltimes in continuous distributed acoustic sensor VSP data: Geophysics, **87**, no. 1, A1–A6, doi: 10.1190/geo2021-0404.1.
Poletto, F., B. Farina, and J. M. Carcione, 2018, Sensitivity of seismic properties to temperature variations in a geothermal reservoir: Geothermics, **76**, 149–163, doi: 10.1016/j.geothermics.2018.07.001.
Quiroga-Goode, G., S. Jiménez-Hernández, M. A. Pérez-Flores, and R. Padilla-Hernández, 2005, Computational study of seismic waves in homogeneous dynamic-porosity media with thermal and fluid relaxation: Gauging Biot theory: Journal of Geophysical Research: Solid Earth, **110**, 1–15, doi: 10.1029/2004JB003347.
Sharma, M. D., 2008, Wave propagation in thermoelastic saturated porous medium: Journal of Earth System Science, **117**, 951–958, doi: 10.1007/s12040-008-0080-4.
Sharma, M. D., 2018, Reflection-refraction of attenuated waves at the interface between a thermo-poroelastic medium and a thermoelastic medium: Waves Random Complex Media, **28**, 570–587, doi: 10.1080/17455030.2017.1370154.
Singh, B., 2011, On propagation of plane waves in generalized porothermoelasticity: Bulletin of the Seismological Society of America, **101**, 756–762, doi: 10.1785/0120100091.
Tzou, D. Y., 1995, A unified field approach for heat conduction from macro- to micro-scales: ASME Journal of Heat Transfer, **117**, 8–16, doi: 10.1115/1.2822329.
Wang, E., J. M. Carcione, J. Ba, and Y. Liu, 2020, Reflection and transmission of plane elastic waves at an interface between two double-porosity media: effect of local fluid flow: Surveys in Geophysics, **41**, 283–322, doi: 10.1007/s10712-019-09572-6.
Wang, E., J. M. Carcione, Y. Yuan, and J. Ba, 2021, Reflection of inhomogeneous plane waves at the surface of a thermo-poroelastic medium: Geophysical Journal International, **224**, 1621–1639, doi: 10.1093/gji/ggaa543.
Wei, W., R. Zheng, G. Liu, and H. Tao, 2016, Reflection and refraction of P wave at the interface between thermoelastic and porous thermoelastic medium: Transport in Porous Media, **113**, 1–27, doi: 10.1007/s11242-016-0659-1.
Youssef, H. M., 2007, Theory of generalized porothermoelasticity: International Journal of Rock Mechanics and Mining Sciences, **44**, 222–227, doi: 10.1016/j.ijrmms.2006.07.001.
Zhou, F., H. Liu, and S. Li, 2019, Propagation of thermoelastic waves in unsaturated porothermoelastic media: Journal of Thermal Stresses, **42**, 1256–1271, doi: 10.1080/01495739.2019.1638333.
Zimmerman, R. W., 2000, Coupling in poroelasticity and thermoelasticity: International Journal of Rock Mechanics and Mining Sciences, **37**, 79–87, doi: 10.1016/S1365-1609(99)00094-5.
Zong, Z., X. Yin, and G. Wu, 2012, AVO inversion and poroelasticity with P- and S-wave moduli: Geophysics, **77**, no. 6, N17–N24, doi: 10.1190/geo2011-0214.1.

Biographies and photographs of the authors are not available.

Downloaded 09/13/24 to 180.201.128.221. Redistribution subject to SEG license or copyright; see Terms of Use at http://library.seg.org/page/policies/terms
DOI:10.1190/geo2023-0625.1